# The influence of Variable Geometry Control on a R290 Ejector Refrigeration System



# The influence of Variable Geometry Control on a R290 Ejector Refrigeration System

**Giorgio Besagni[1], Fabio Inzoli[1]**

[1]Politecnico di Milano, Department of Energy, via Lambruschini 4a, 20156, Milano (Italy)

giorgio.besagni@polimi.it

**Abstract**. The large-scale deployment of ejector refrigeration systems (i.e., solar-based ejector refrigeration systems), although representing a promising alternative compared with mechanical compressor ones, is hindered due to limitations regarding ejector control modes. Indeed, ejectors are fluid-dynamics controlled devices and, because of their fixed geometry, they operate at their highest efficiency in a narrow range of operating conditions, which is in contrast with the dynamic pressure and temperature levels characterizing real applications. In this context, variable geometry ejectors (*VGE*) represent a promising solution to increase the flexibility and operation range of this component. The present study aims to extend the present body of knowledge regarding *VGE* systems, evaluating the impact of a spindle-provided ejector operated with R290 on the performance of the refrigeration system. The analysis has been carried out using an integrated lumped parameter/*CFD* approach, thus linking the local flow properties and global performances. Different spindle positions have been tested to assess how the different nozzle area ratios affect both the entrainment ratio and the critical pressure. Results showed that increasing primary nozzle area ratio the system can effectively reduce the thermal input, increasing the average *COP* at the expanse of a lower critical pressure. In conclusion, using a moving spindle control system might ensure an improvement of the ejector performance.

## 1. Introduction

Ejector is a device constituted by a primary nozzle, a suction chamber, a mixing chamber, and a diffuser, whose main geometrical parameters are presented in Figure 1. The "*high energy*" primary flow accelerates and expands through the primary nozzle creating a low-pressure region nearby the nozzle exit; subsequently, the secondary flow is entrained into the mixing chamber because of the vacuum-effect and the shear action between the primary and secondary flows. The primary and the secondary flows mix within the mixing chamber and the resulting stream moves into a diffuser where the high velocity fluid is gradually decelerated and increased in pressure due to subsonic conditions.

The entrainment, the pressure recovery, and the mixing effects provided by the ejector, makes it suitable to be employed in ejector refrigeration systems (*ERSs*; Figure 2a presents the layout of a standard ejector refrigeration system, *SERS*) [1]. In general, *ERSs* are promising alternative compared with compressor-based technologies owing to their reliability, limited maintenance, low initial and operational costs, and no working fluid limitations [2]; also, the generator of an *ERS* might exploit low-grade heat energy, making *ERSs* valuable in contributing towards reducing electricity consumption in the residential sector [3].

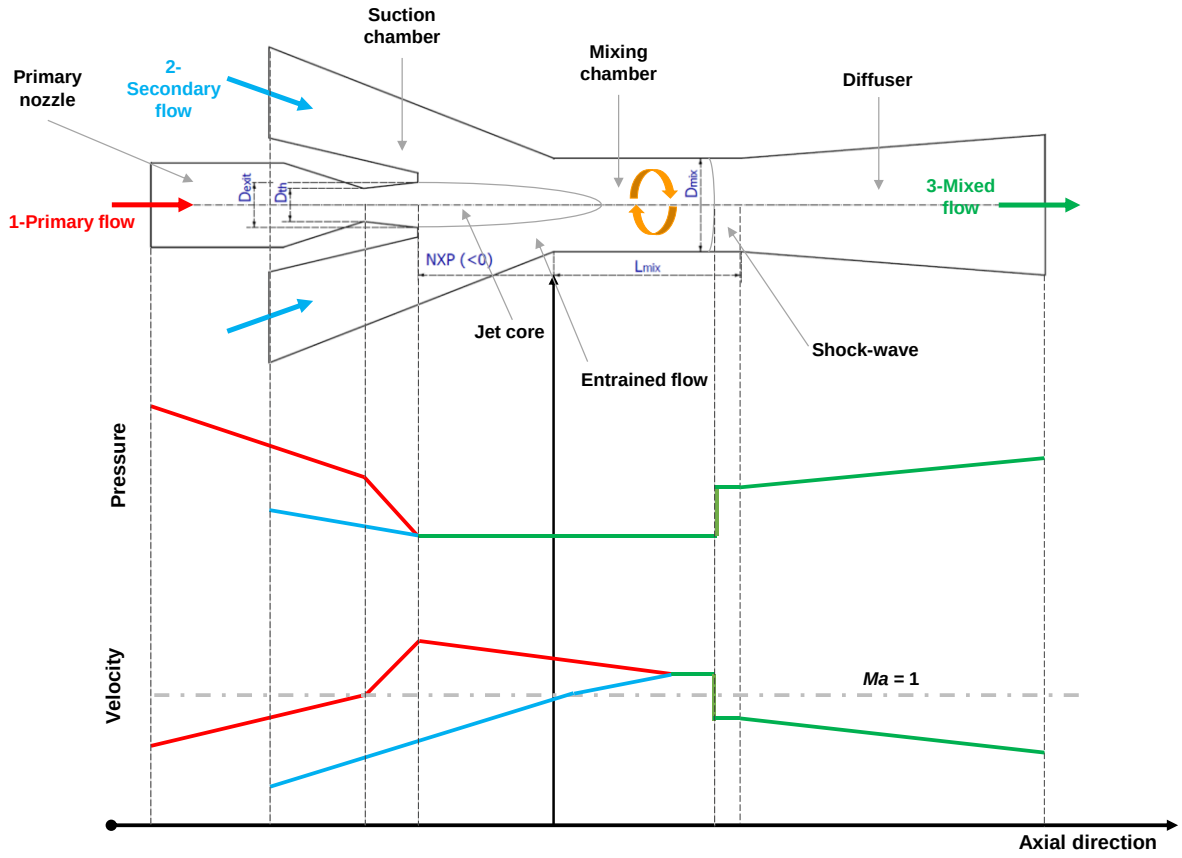


**Figure 1.** Ejector design and qualitative axial pressure and velocity trends

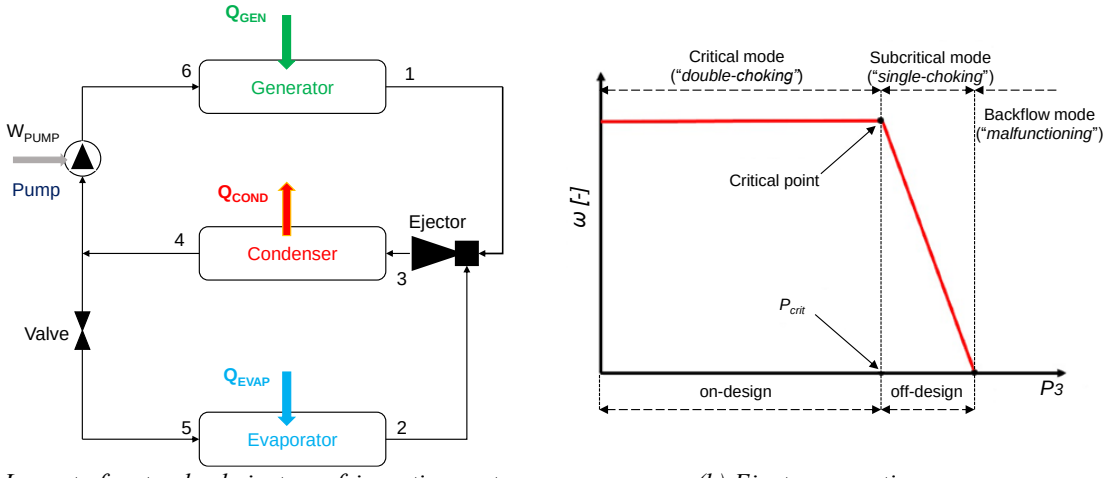


*(a) Layout of a standard ejector refrigeration system* *(b) Ejector operating curve*

**Figure 2.** Ejector component (a) and ejector refrigeration system (b)

Unfortunately, the large-scale deployment of *ERSs* is hindered owing to two main drawbacks: the low coefficient of performance (in the range of 0.1–0.7) and the relevant influence of ejector operation on the performance of the whole system. The latter can be easily explained by the fact that the ejector is a fluid-dynamics controlled device, where the fluid-dynamic interactions at the "*local-scale*" impact on the performances at the "*component-scale*", namely the entrainment ratio $\omega$ (viz- the ratio between secondary and primary mass flow rates, Figure 2b). These multi-scale relationships can be easily explained considering that the ejector operation relies on two concurrent physical phenomena: (i) the

low-pressure fluid entrainment process caused by the primary flow expansion and (ii) the compression effect, provided by the diffuser, which raises the secondary flow pressure from the evaporator to the condenser pressure. These two effects are contrasting, and an improvement of the former would deteriorate the latter: hence, for a given nozzle area ratio, the ejector operating curve is imposed by the primary and secondary flow boundary conditions. On the other hand, Variable Geometry Ejectors (*VGE*) represent a promising solution to increase the flexibility and operation range of this component. In a *VGE*, the spindle acts on the nozzle area, and primary flow rate, and changes the ejector's response by adjusting its entrainment ratio accordingly with the requirements of the system. (i.e., temperature set point, thermal load, …).

The present-day discussion regarding ejector technology is even more challenging owing to the current transition in refrigerants; given the European regulation aimed to limit the emission of fluorinated greenhouse gases, the existing market is expected to change sharply in the next years, and 3$^{rd}$ generation refrigerants (i.e., R134a) will be most likely replaced by natural (i.e., hydrocarbons) and 4$^{th}$ generation fluids (i.e., hydrofluoroolefins) [4]. Among the new refrigerants, *R290* (propane) is promising owing to its favourable thermodynamic properties, which make it suitable for refrigeration applications in the medium-long views.

This paper aims at extending knowledge on *VGE* systems, evaluating the impact of a spindle-provided ejector operated with R290 on the performance of an *ERS*. The present paper employs a multi-scale concept, by using an integrated Computational Fluid Dynamic (*CFD*) - Lumped Parameter Model (*LPM*) of the *ERS*. The *CFD* approach solves the fluid-dynamics within the ejector ("*local-scale*") and provides the ejector entrainment ratio ("*component-scale*"). Conversely, the refrigeration cycle ("*system-scale*") has been modelled by a *LPM* approach using as input data *CFD* outcomes.

## 2. Methods

### *2.1. Test case*

The tested ejector has been derived from Del Valle et al. [5] and has been already employed in the previous screening of new refrigerants and ejector design sensitivity analysis in Besagni et al. [6]. It should be noted how, compared with the latter reference, the mixing chamber diameter has been reduced to 4 mm to extend the on-design operating mode. The present ejector has been provided of a spindle (Figure 3) which can move axially within the primary nozzle. The neutral spindle position (*SP*) in which the tip of the spindle is placed right in the nozzle throat has been named as *SP*#0. Moving the spindle towards the nozzle exit, the nozzle throat area is reduced, and the area ratio is increased. The effects of the *SP* have been analyzed in the range 0-7 mm, with a discretization of 1 mm each position, whose code name will be referred as *SP#0..7*, depending on the *s*pindle position. A 2D axysimmetric geometrical model has been designed and discretized according to the mesh criteria defined in ref. [7], with an average cell number of 228,000 after the double cycle mesh adaption.

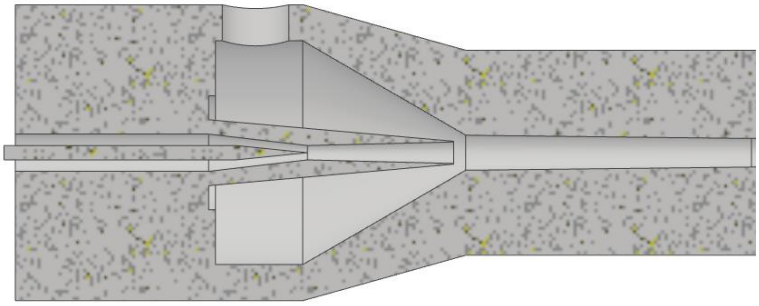

**Figure 3.** Ejector primary nozzle equipped with the spindle

Propane (*R290*) has been selected as refrigerant and the ejector has been tested with fixed thermodynamic conditions (temperature and pressure) at primary and secondary inlet. Primary inlet

superheating has been set equal to 10°C, while secondary superheating has been set equal to 4°C to avoid condensation inside the ejector.

Table 1 summarizes the inlet boundary conditions (T and P), the max value of outlet pressure ($P_{3max}$) and the critical pressure ($P_{3crit}$). Modifying the spindle position and varying the pressure outlet condition the VGE's operating curves has been obtained. The critical conditions has been obtained with an iterative approach.

**Table 1.** Boundary conditions of the simulated cases; the primary flow is labelled as 1, the secondary flow 2 and the outlet stream 3 (Figure 2a)

| ***Code name (spindle position)*** | $T_1$ **[°C]** | $P_1$ **[kPa]** | $T_2$ **[°C]** | $P_2$ **[kPa]** | $P_{3,crit}$ **[kPa]** | $P_{3,max}$ **[kPa]** |
|---|---|---|---|---|---|---|
| SP#0 | 84.2 | 2,813.5 | 14 | 636.6 | 1,014.1 | 1,052.7 |
| SP#1 | 84.2 | 2,813.5 | 14 | 636.6 | 1,009.0 | 1,039.7 |
| SP#2 | 84.2 | 2,813.5 | 14 | 636.6 | 988.9 | 1,026.8 |
| SP#3 | 84.2 | 2,813.5 | 14 | 636.6 | 961.8 | 1,014.0 |
| SP#4 | 84.2 | 2,813.5 | 14 | 636.6 | 918.6 | 964.2 |
| SP#5 | 84.2 | 2,813.5 | 14 | 636.6 | 869.9 | 916.2 |
| SP#6 | 84.2 | 2,813.5 | 14 | 636.6 | 806.0 | 836.5 |
| SP#7 | 84.2 | 2,813.5 | 14 | 636.6 | 731.5 | 772.3 |

*2.2. Numerical modelling*

The finite volume code ANSYS Fluent (*Release 2020 – R1*) has been used to solve the 2-D axysimmetric steady-state Reynolds Averaged Navier-Stokes (*RANS*) equations for the turbulent compressible Newtonian flow, employing *k-ω SST* as turbulence model [7]. To limit the numerical diffusion, second-order upwind numerical schemes have been used for the spatial discretization, except for the pressure equation. In this case, PRESTO! scheme has been chosen since it is designed for flows involving steep pressure gradients. Second-order upwind schemes also for the turbulence model variables have been used. Gradients are evaluated by a least-squares approach. The initialization has been performed by a two-step approach: (i) a hybrid initialization followed by a (ii) full multi-grid (*FMG*) scheme. Pressure-based solver with Coupled algorithm has been adopted since it is described by Croquer et al. [8] as far more stable than density based-solver nevertheless sufficiently accurate and suitable for high-velocity compressible flows. Pseudo-transient option was enabled, which was found to speed up the steady-state solution. R290 properties have been evaluated with the real-gas NIST database. Ejector inlets boundary conditions are prescribed in terms of total pressure and temperature, while the turbulence boundary conditions have been implemented as hydraulic diameter and the turbulent intensity (5% for the primary flows and 2% for the secondary one) [7]. Outlet condition has been modelled as a pressure boundary condition.

*2.3. Multi-scale modelling*

The above-described *CFD* model is used to solve the "*component-scale*" (viz., the entrainment ratio $\omega$) and the fluid-dynamics ("*local-scale*"). Once such information is derived, the ejector component is then included within a refrigeration cycle, which is modelled by a *LPM* approach, to estimate the "*system-scale*" performances. The considered cycle has been the *SERS* architecture (Figure 2a) since it is the elementary scheme and, thus, its results could be extended to any other derived system. The advantage of such approach is to consider the fluid dynamics phenomena within the cycle performances. *SERS* input data concern (i) $P_1$, $T_1$, $P_2$, $T_2$ and $P_3$, which act as boundary conditions for the *CFD* simulations, and (ii) the mass flow rates $\dot{m}_1$ and $\dot{m}_2$ and $T_3$, which are the *CFD* model output. To model the *SERS*, the prevailing assumption concerns the absence of pressure losses within the heat exchangers, so to relate ejector boundary conditions to the cycle pressure and pressure levels (Figure 2a). Given the ejector boundary conditions, the thermodynamic points of the *SERS* cycle have been obtained; in particular, in this process, the pump has been modelled considering an isentropic

efficiency equal to 0.9.[6]. After all thermodynamic points of the *SERS* cycle have bene obtained, the cooling power ($\dot{Q}_{evap}$), input thermal power ($\dot{Q}_{gen}$) and electrical power required by the pump ($\dot{W}_{pump}$) are computed using the mass flow rates $\dot{m}_1$ and $\dot{m}_2$, which are *CFD* model output:

$$\dot{Q}_{evap}=\dot{m}_2(h_2-h_5) \quad (1)$$

$$\dot{Q}_{gen}=\dot{m}_1(h_1-h_6) \quad (2)$$

$$\dot{W}_{pump}=\dot{m}_1(h_6-h_4) \quad (3)$$

Then the cycle *COP* is computed as:

$$COP=\frac{\dot{Q}_{evap}}{\dot{Q}_{gen}+\dot{W}_{pump}} \quad (4)$$

Coupling Eqs. (1-3) with Eq. (4), it follows:

$$COP=\omega\frac{h_2-h_5}{h_1-h_4} \quad (5)$$

Based on Eq. (5) it is worth noting that COP is related to $\omega$, thus linking ejector performances ("*component-scale*") and the system *COP* ("*system-scale*").

## 3. Results

*SERS* performances have been computed based on the modelling approach described in Section 2.3, whereas the outcomes are presented in Figures 4-9. Figure 4 displays the ejector operating curves for the different spindle positions and the critical point operation is highlighted in red. Figure 5 displays the relationship between the spindle position and the primary and secondary mass flow rates as well as the generator and evaporator thermal powers (Eqs. (1-2)), for the ejector operated in the critical conditions. Figure 6 displays the relationship between the spindle position and ejector $\omega$ and $P_{crit}$, and system *COP* are presented. for the ejector operated in the critical conditions. Figure 7 displays the *SERS P-h* representations and Figures 8 and 9 display and the Mach contours of the flow fields within the ejector at the critical conditions.

Looking at Figure 4, it is noted that when moving the spindle towards the mixing chamber, $\omega$ is increased, but $P_{crit}$ is decreased, limiting the maximum allowable condenser temperature. This effect can be explaining by considering that the spindle position affects the primary and secondary mass flow rates: the former decreases as the spindle moves towards the nozzle exit, whereas the latter is slightly increased (Figure 5). Indeed, shifting the spindle inside the nozzle, the nozzle throat area is reduced and so does the primary mass flow rate (related to the generator thermal power); the trend is not linear with the spindle position, as the nozzle throat area is ring-shaped, hence the first positions of the spindle have a smaller impact on ejector performances than the following ones. Although less pronounced than the primary mass flow rate change, the increase in secondary mass flow rates is caused by the different expansion of the primary jet (Figure 8 and Figure 9). An increase in the nozzle area ratio leads the primary flow to a more pronounced contraction of the jet core, which frees more cross-section area to secondary flow entrainment. The concurrent increase of secondary flow rate and decrease of the motive one results in a noticeable improvement of the ejector entrainment ratio (Figure 6). It should be noted that the higher entrainment performance is countered by a lower $P_{crit,}$ (Figure 4 and Figure 6) which is found to be reduced when the spindle is moved towards the nozzle exit position: moving the spindle from 0 to 7 mm ω is increased by 85.8% while the $P_{crit}$ is reduced by 283 kPa. The above-reported improvement of the ejector entrainment ratio, moving the spindle toward the nozzle exit position, can also be observed by considering the changes in the thermodynamic representation of the cycle (Figure 7, comparing *SERS P-h* at critical conditions for *SP#0* and *SP#7*).

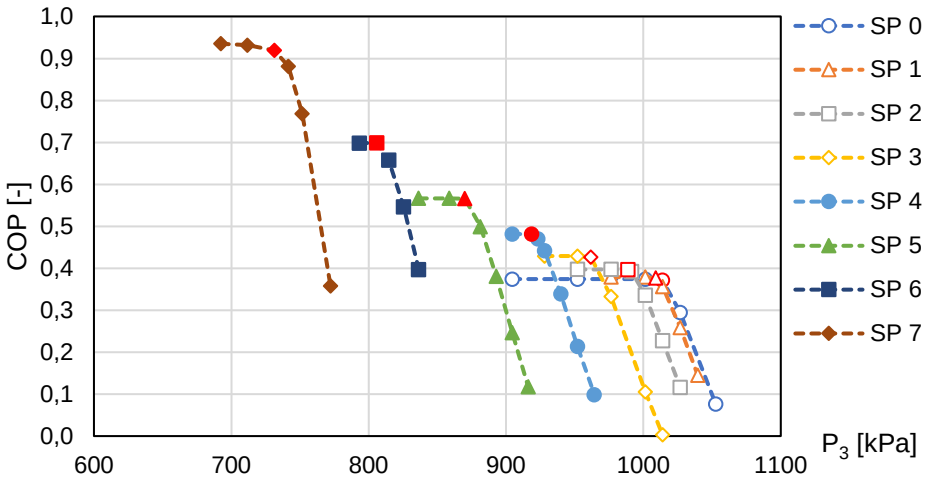


**Figure 4.** Ejector operating curves for the different spindle positions

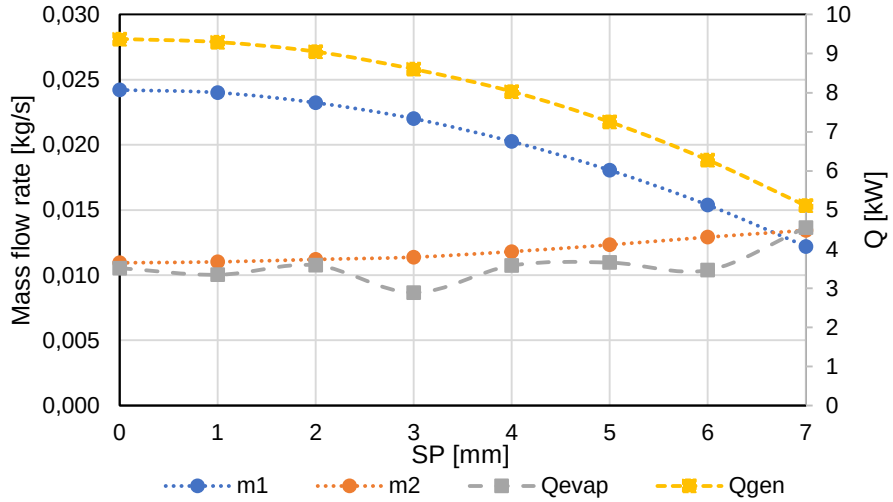


**Figure 5.** The effect of the Spindle position on mass flow rates and thermal power (critical condition)

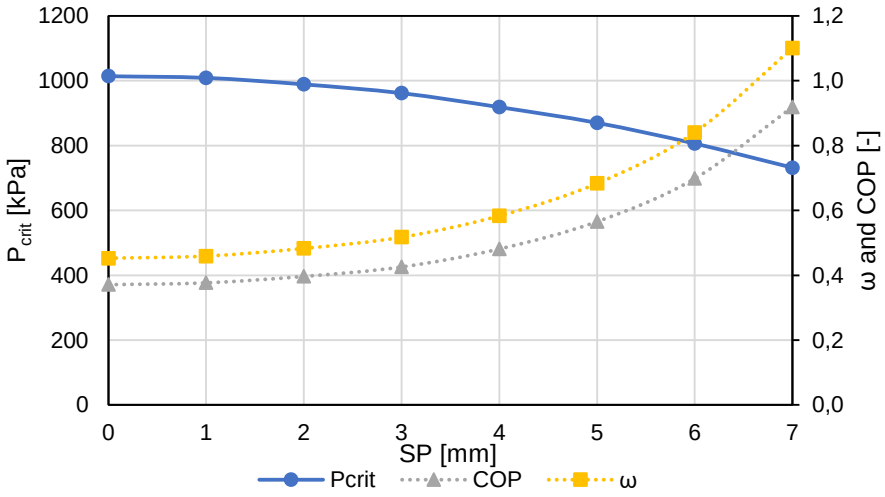


**Figure 6.** The effect of the Spindle position on $P_{crit}$, ω and COP (critical condition)

The different spindle positions affect the two main performance parameters of ejectors, namely ω and $P_{crit,}$ which influence the system performance, in turn. $\omega$ directly influences the *COP* of the cycle, as it can be concluded by observing the *COP* definition as a function of the cycle properties. $P_{crit}$, instead, not only affects the maximum allowable condenser temperature of the system for which the ejector works at its best efficiency in the double-chocking operating mode but has a lower impact on the cooling capacity, too (Figure 7), the lower condenser temperature for the ejector used with *SP#7* mm (owing to the lower $P_{crit}$), results in a different positioning of point# 4,5,6 which are shifted toward the left part of the *P-h* diagram. This causes the specific generator input and the specific cooling capacity to increase with the result that their ratio; It should also be noted that the cooling power, is also increased because of the higher secondary mass flow rate $\dot{m}_2$.

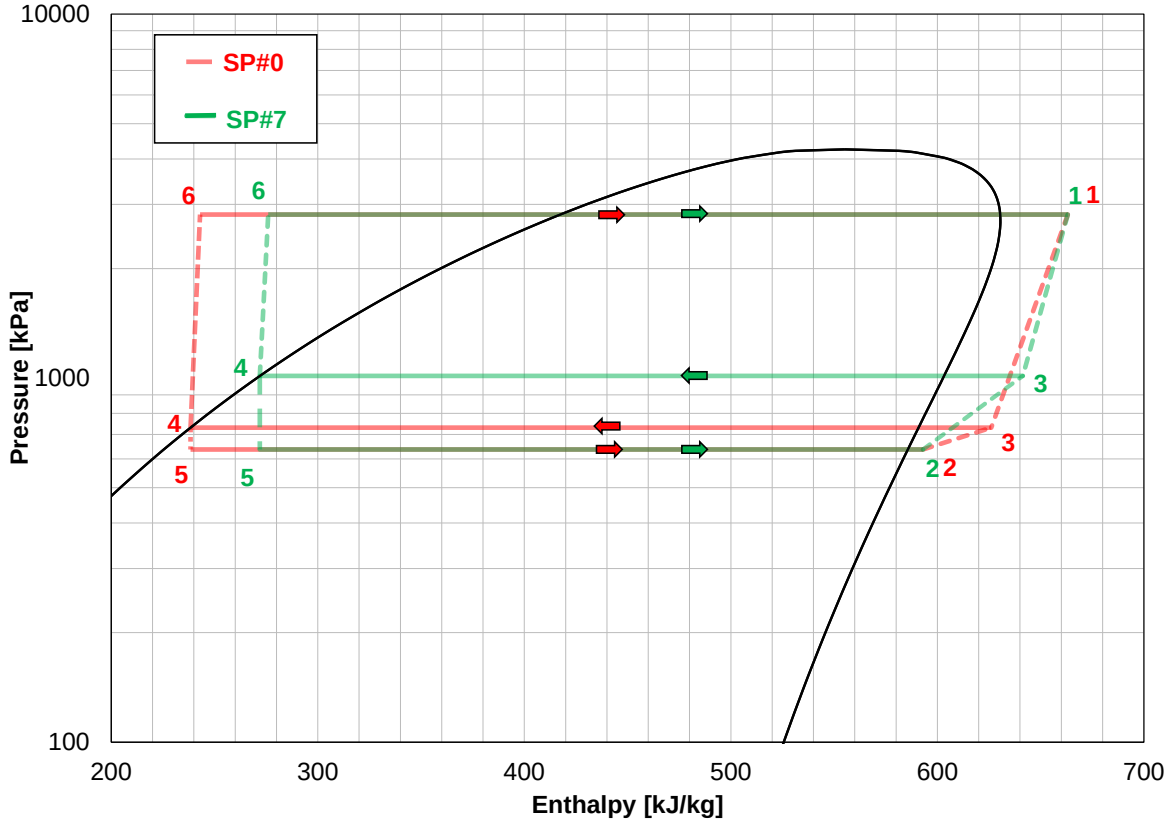


**Figure 7.** *SERS P-h* representations of *SP#0* and *SP#7* at the ejector critical conditions (Figure *4*)

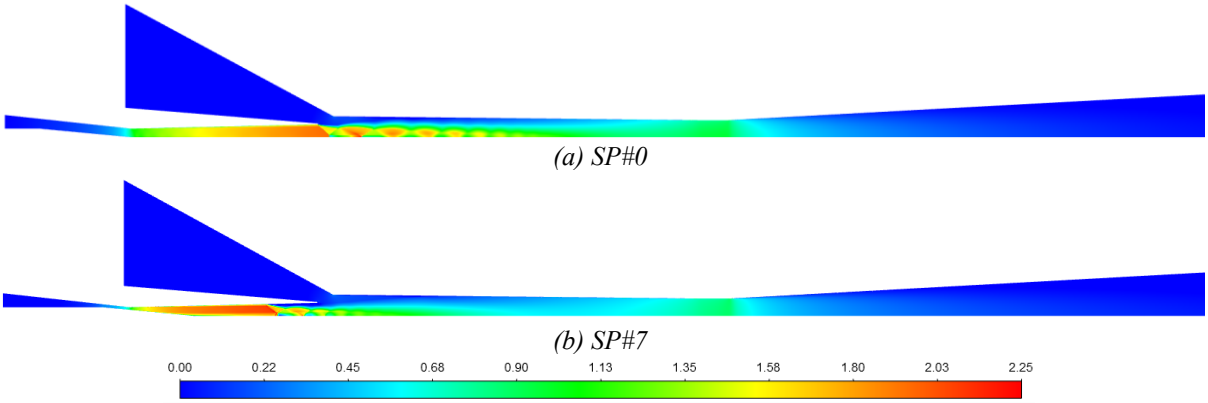


*(a) SP#0*

*(b) SP#7*

**Figure 8.** Ejector flow fields (Mach number contours) *of SP#0 and* SP#7 at the ejector critical conditions (Figure 4)

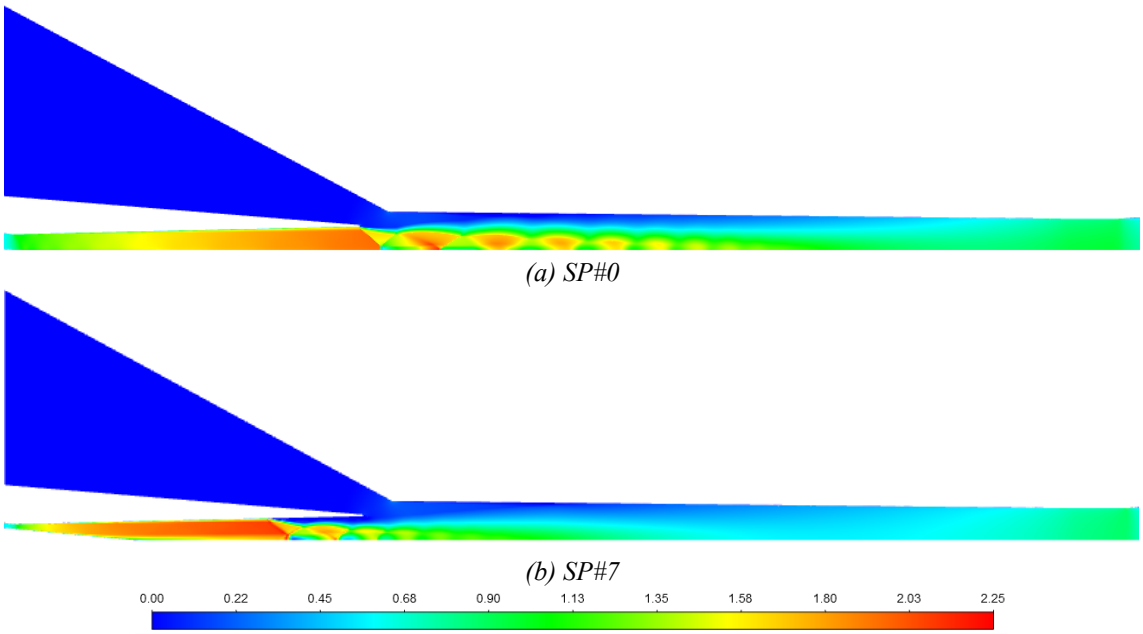


**Figure 9.** Ejector flow fields (Mach number contours) *of SP#0 and* SP#7 at the ejector critical conditions (Figure 4) – closer look at the nozzle exit position

## 4. Conclusions

In this paper, a multi-scale numerical study of a *VGE* operated with R290 has been presented. A *CFD* model has been used to solve the fluid-dynamics within the ejector ("*local-scale*") and to provide the ejector performances ("*component-scale*"). Conversely, the *SERS* performance ("*system-scale*") has been modelled by a *LPM* approach using as input data *CFD* outcomes. It is noted that, when moving the spindle towards the mixing chamber, ω is increased because of the primary flow rate reduction, but $P_{crit}$ is decreased, limiting the maximum allowable condenser temperature. In conclusion, using a moving spindle control system might ensure an improvement of the ejector performance; this is of practical use, for example, when the condenser saturation pressure decreases (i.e., owing to a lower solar heat source). Future works will be devoted to developing dynamic look-up tables to be implemented in a variable ejector control system.

## 5. Acknowledgment

Authors are grateful to Nicolò Cristiani, for the meaningful discussions and for his valuable support.

## 6. References

[1] Aidoun Z, Ameur K, Falsafioon M and Badache M 2019 *Inventions* **4** 15
[2] Besagni G, Mereu R and Inzoli F 2016 *Renew. Sust. Energ. Rev.* **53** 373-407
[3] Knobloch F, Pollitt H, Chewpreecha U, Daioglou V and Mercure J F 2019 *Energ. Effic.* **12**(2) 521-550
[4] Cavallini A 2020 *J. Phys. Conf. Ser.* **1599** 012001
[5] Del Valle J G, Jabardo J S, Ruiz F C and Alonso J S J 2014. *Int. J. Refrig.* **46** 105-113
[6] Besagni G, Cristiani N, Croci L, Guédon G R and Inzoli F 2021 *Appl. Therm. Eng.* **186** 116502
[7] Besagni G, Cristiani N, Croci L, Guédon G R and Inzoli F 2021 *Appl. Therm. Eng.* **186** 116431
[8] Croquer S, Poncet S and Aidoun Z 2016 *Int. J. Refrig.* **61** 140-52